Physics Letters B 743 (2015) 310–314

Contents lists available at ScienceDirect

Physics Letters B

www.elsevier.com/locate/physletb

# Neutron interferometry constrains dark energy chameleon fields

H. Lemmel [a,b], Ph. Brax [d], A.N. Ivanov [a], T. Jenke [a], G. Pignol [c], M. Pitschmann [a], T. Potocar [a], M. Wellenzohn [a], M. Zawisky [a], H. Abele [a,*]

[a] Technische Universität Wien, Atominstitut, 1020 Wien, Austria
[b] Institut Laue-Langevin, 38042 Grenoble, France
[c] LPSC, Université Grenoble Alpes, CNRS/IN2P3 F-38026 Grenoble, France
[d] Institut de Physique Théorique, CEA, IPhT, CNRS, URA 2306, F-91191 Gif/Yvette Cedex, France

ARTICLE INFO

*Article history:*
Received 19 January 2015
Received in revised form 20 February 2015
Accepted 24 February 2015
Available online 5 March 2015
Editor: V. Metag

*Keywords:*
Chameleon field
Dark energy
Neutron interferometry

ABSTRACT

We present phase shift measurements for neutron matter waves in vacuum and in low pressure Helium using a method originally developed for neutron scattering length measurements in neutron interferometry. We search for phase shifts associated with a coupling to scalar fields. We set stringent limits for a scalar chameleon field, a prominent quintessence dark energy candidate. We find that the coupling constant $\beta$ is less than $1.9\times10^7$ for $n=1$ at 95% confidence level, where $n$ is an input parameter of the self-interaction of the chameleon field $\varphi$ inversely proportional to $\varphi^n$.



## 1. Introduction

The accelerating expansion of the universe suggests that most of the energy in the universe is 'dark energy'. The nature and origin of this energy remain unknown. Candidates for dark energy are either Einstein's cosmological constant or dynamical dark energy, i.e. the so-called quintessence canonical scalar field $\varphi$, responsible for the late–time acceleration of the universe expansion. Chameleon fields are a prime example of dynamical dark energy. Their effective mass depends on the energy density of matter in which it is immersed [1]. As a result, in a sufficiently dense environment the chameleon field is very massive and, correspondingly, substantially Yukawa-suppressed, i.e. very short-ranged. In turn, it is essentially massless on cosmological scales [2,3]. Because of its sensitivity on the environment, such a mass-changing scalar field has been called *chameleon*. Moreover, the chameleon field always couples to matter and generates a fifth force with an effective range inversely proportional to its effective mass.

All models of dark energy involve a light scalar field [1,2] whose effects on solar system tests of gravity needs to be shielded. Three main screening mechanisms [3] have been unraveled so far. The K-mouflage and Vainshtein screenings are very powerful inside a large domain surrounding the earth, rendering their test in laboratory experiments extremely arduous. On the other hand, the chameleon mechanism is at work in the presence of dense objects and can be tested in near-vacuum experiments [4]. This is the case for the Eotwash [5] and Casimir experiments [6], where the boundary plates are screened. Another way of testing the chameleon mechanism involves small and unscreened objects, like neutrons under certain conditions [7].

Concerning chameleon models, a chameleon–photon coupling $g_{\rm eff}=\beta_\gamma/M_{\rm Pl}$ has been proposed, and the detailed analysis of the chameleon–photon interaction and a comparison with the cosmological data has been carried out in [8–12]. A search for photon–chameleon–photon transition has been performed by the experiment CHASE (the GammeV CHameleon Afterglow SEarch) [13] and by the Axion Dark Matter eXperiment (ADMX) [14]. A search for chameleon particles created via photon–chameleon oscillations within a magnetic field is described in [15].

Searches with neutrons directly test the chameleon–matter interaction $\beta$ and do not rely on the existence of a chameleon–photon interaction. The coupling $\beta$ is restricted from below, e.g. $\beta$ must be larger than 50 at $n=1$ [16], and experiments with neutrons have the potential ultimately to find a chameleon field or exclude it in the whole parameter space.

As it has been pointed out by Pokotilovski [17], the use of a neutron Lloyd's interferometer for measurements of the phase-shift of the wave function of cold neutrons should allow to determine the chameleon–matter coupling constant. The *q*BOUNCE Collaboration has searched for the chameleon field using gravity resonance spectroscopy and ultra-cold neutrons [18–21]. In a recent

* Corresponding author.
*E-mail address:* abele@ati.ac.at (H. Abele).

http://dx.doi.org/10.1016/j.physletb.2015.02.063

experiment [22], the upper limit for $\beta$ has been determined as $\beta < 5.8 \times 10^8$ which is five orders of magnitude below the previous limit determined by atomic spectra [16].

Here we present a new search for chameleon fields by means of neutron interferometry as proposed in [7]. The self-interaction of the chameleon field $\varphi$ and its interaction to an environment with mass density $\rho$ are described by the effective potential [23,24]

$$\mathcal{V}_{\text{eff}}(\varphi) = \frac{\Lambda^{n+4}}{\varphi^n} + \frac{\beta\,\rho\,\hbar^3 c^3 \varphi}{M_{\text{Pl}}}, \tag{1}$$

where $\beta$ is the coupling constant, $n$ is an input parameter (the so-called Ratra–Peebles index) and $\Lambda \approx 2.4 \times 10^{-12}$ GeV defines an energy scale [7]. $M_{\text{Pl}} = \sqrt{\hbar c/(8\pi G)} = 4.341 \times 10^{-9}$ kg denotes the reduced Planck mass. The chameleon field $\varphi$ creates a potential for neutrons given by $V = \beta\,\varphi\, m/M_{\text{Pl}}$ where $m$ denotes the neutron mass. When passing this potential, neutrons accumulate the phase

$$\zeta = -\frac{m}{k\hbar^2}\int V(x)\,dx = -\frac{m}{k\hbar^2}\int \beta\frac{m}{M_{\text{Pl}}}\varphi(x)\,dx, \tag{2}$$

where $k$ denotes the neutron wave vector modulus $k = 2\pi/\lambda$.

For strong coupling ($\beta \gg 1$) the chameleon field is suppressed at the presence of matter, even at low mass densities like air at ambient pressure. Only in vacuum the chameleon field can persist. By placing a vacuum cell into one arm of the neutron interferometer and allowing ambient air in the other arm we can directly probe the chameleon field. The setup resembles a standard setup for measuring neutron scattering lengths [25], but instead of measuring the phase shift of sample material we measure the phase shift of vacuum.

The chameleon field vanishes at the walls of the vacuum chamber but increases bubble-like towards the middle of the chamber, cf. Fig. 1 (c). The lower the remaining gas pressure is, i.e. the better the vacuum, the more the field increases. Thus we have two options of performing a relative phase measurement which is necessary to cancel the unknown intrinsic interferometer phase and the air phase shift. In the pressure mode we vary the pressure in the vacuum cell by letting in different amounts of Helium. In the profile mode we keep the pressure constant but move the chamber transversally to the beam in order to record a profile of the chameleon bubble. Neither method detects any chameleon-like signature, giving rise to new constraints of the chameleon theory.

## 2. Setup

The experiment is carried out at the neutron interferometry setup S18 at the Institut Laue-Langevin (ILL) in Grenoble. A perfect crystal silicon interferometer is used, Fig. 1 (a), at 45° Bragg angle and 2.72 Å mean wave length $\lambda$ with 0.043 Å wavelength distribution width (FWHM). The two beam paths within the interferometer are separated by 50 mm over a length of 160 mm. Neutron detectors with an efficiency above 99% measure the intensities of the two exit beams labeled O and H respectively. A vacuum chamber with inner dimensions $40 \times 40 \times 94$ mm is inserted in the left or right beam path. The other beam path always contains one of the two air chambers which sit alongside the vacuum chamber. The whole chamber box can be moved sidewards for swapping the vacuum cell between the left and the right beam path and to probe different beam trajectories within the vacuum cell. The air chambers ensure that both beam paths contain the same amount of wall material (aluminium). In addition, the extension of the vacuum cell by air chambers minimizes possible disturbances of the thermal environment of the crystal when the chamber box is moved. We label different chamber positions by the letters 'a' to 'n' as indicated in the figure.

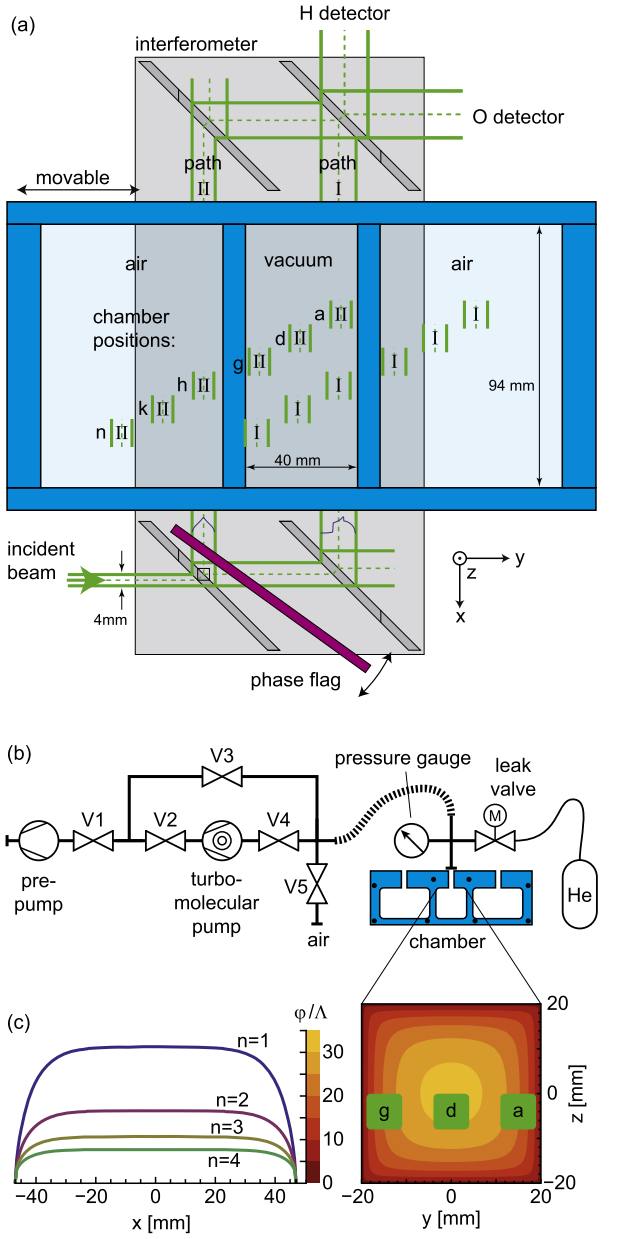


**Fig. 1.** (a) Top view of the interferometry setup shown in chamber position 'h'. The chamber box (blue) can be moved transversally allowing the beams to pass at different positions, labeled by 'a' to 'n'. (b) Scheme of the vacuum handling and axial view of the vacuum chamber. (c) Longitudinal and transverse bubble shape of the chameleon field in the vacuum cell. The beam positions 'a', 'd' and 'g' are indicated by green rectangles. (For interpretation of the references to color in this figure legend, the reader is referred to the web version of this article.)

The air chambers are connected to ambient air by a hole in the top of the chambers. The vacuum chamber is connected to a vacuum control system consisting of pressure gauge, motorized leak valve and pumps, as indicated in Fig. 1 (b). The pumps (pre-pump and turbomolecular pump) are running continuously while a controlled amount of Helium is let in through the leak valve in order to tune the pressure. The pressure gauge is corrected for the use with Helium.

## 3. Data acquisition and evaluation

Phases in neutron interferometry are measured by rotating an auxiliary phase flag and recording the intensity oscillations be-

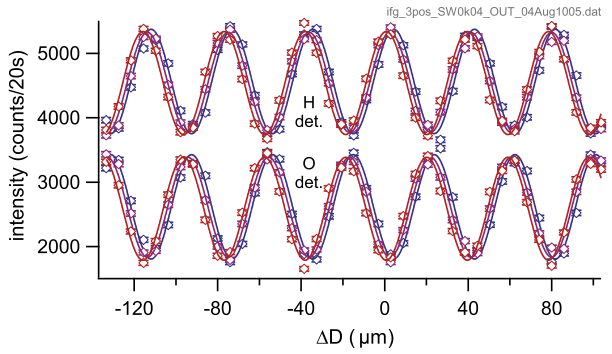


**Fig. 2.** Recorded intensity oscillations between O and H detector as a function of the optical path length difference $\Delta D$ created by rotating the phase flag. The three curves in red, purple and blue represent the interferograms at the 'a', 'd' and 'g' position respectively. The phase shift between these raw curves is created by position dependent wall thickness variations, cf. Fig. 3. (For interpretation of the references to color in this figure legend, the reader is referred to the web version of this article.)

tween O and H detector, cf. Fig. 2. Such interferograms are measured before and after some parameter change. The shift of the sine curves with respect to each other represents the phase shift induced by the parameter change. The recording of each interferogram takes typically half an hour, and during that time the intrinsic phase of the interferometer can drift due to temperature changes or other environmental factors. To compensate such drifts we interlace phase flag movement and parameter change. The phase flag is rotated to the first angular position and neutrons are counted for a certain amount of time for each parameter setting. Then the phase flag is rotated to the next position and neutrons are counted again for all parameter settings etc. In the end we obtain interferograms measured simultaneously for all parameter settings. Their relative phases are free of phase drifts.

We use the largest neutron interferometer available [26] with a loop size of 50 × 160 mm in order to maximize the size of the vacuum cell. Such big single crystal interferometers are extremely sensitive to temperature gradients, air flow, vibrations, bending, etc. Hence the interference contrast (fringe visibility) is restricted to about 10% to 30%. The interferograms look a bit more noisy than what can be explained by pure counting statistics. This means that the phase is slightly fluctuating within the recording time of each interferogram. We conservatively account for this noise by performing a $\chi^2$ test for each sine fit and by blowing up the fit error (by a factor of about 2) such that the $\chi^2$ test is satisfied.

### 3.1. Profile mode

In the profile mode we measure at up to 14 transverse beam positions for each phase flag position in order to look for bubble-like phase profiles. Ideally, the entry and exit walls of the vacuum chamber are flat and parallel and therefore would not alter the phase if the chamber is transversally moved. Unfortunately, the screw holes of our walls have been drilled after the surfaces had been polished. As a consequence, the surfaces are elevated by a few microns around each screw hole, and all our data in profile mode require a position dependent phase correction, based on a careful mapping of the wall thickness, as indicated in Fig. 3 (a) and (b). The screw hole positions are indicated by black dots in Fig. 3 (a) and Fig. 1 (b). Fortunately, the correction depends mainly linear on the beam position, while the shape of the chameleon bubble is expected to be mainly parabolic. To be precise, the chameleon profile must be symmetric with respect to the cell center, and can therefore consist only of quadratic and higher even orders. Thus, there is no danger that the wall thickness correction

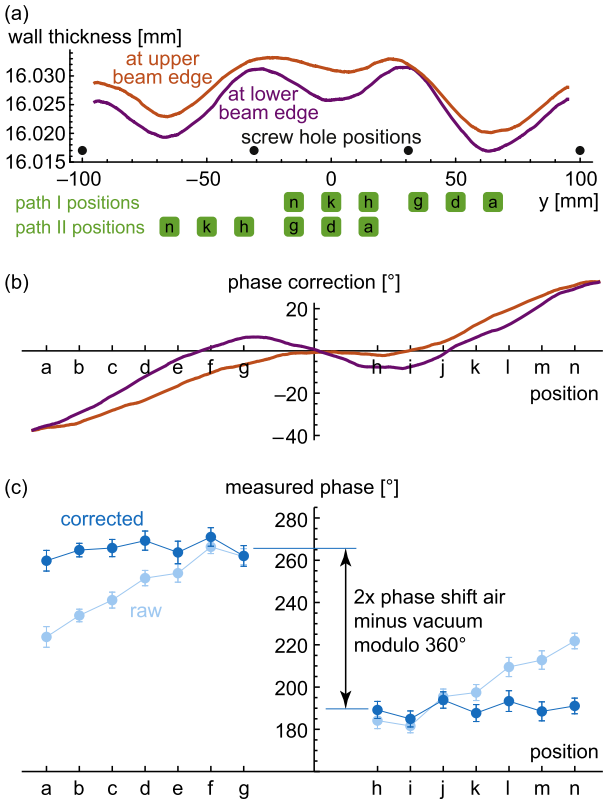


**Fig. 3.** (a) Mechanical measurement: measured total thickness of the entry and exit walls at two different vertical positions. The thickness is increased around the screw holes (black dots). The positions of beam path I and II are indicated for several chamber positions. (b) Phase shift calculated from (a), caused by the different amount of wall material (aluminium) in path I and II for different chamber positions. (c) Phase profile of the vacuum chamber with and without correction for the wall thickness. On the left side (a–g) path I passes air and path II passes vacuum; vice versa on the right side.

completely mimics or hides the chameleon feature. We determine the thickness correction at the upper and the lower edge of the beam, and use the average as correction and a quarter of the difference as uncertainty of the correction.

Fig. 3 (c) shows the recorded phase over a complete profile. In position 'a' to 'g' path I passes air and path II passes vacuum while in position 'h' to 'n' it is the other way round, cf. Fig. 1 (a). The slope within each group is caused by the thickness variation of the chamber walls. The step between the two groups comes from the sign change of the air phase shift when air and vacuum are swapped between the beam paths.

The height of the chameleon bubble can be determined by comparing the phase at the center of the chamber with the phase at its side, close to the chamber walls. Therefore we make most of our measurements at positions 'a', 'd' and 'g'. Fig. 4 (a) summarizes the result of the bubble height measurements for various pressure settings. The statistical error of the phase can be reduced to typically 0.9° by averaging over 15 measurements. However, the thickness correction, which is applied after the statistical averaging, increases the error again to typically 2.5°.

### 3.2. Pressure mode

In the pressure mode we apply four different pressures at each phase flag position. A quick pressure change is only possible in the pressure range of the turbomolecular pump, i.e. below $10^{-2}$ mbar. The average of four such runs is shown in Fig. 4 (b). In order to compensate phase drifts we use the phase at the highest pressure

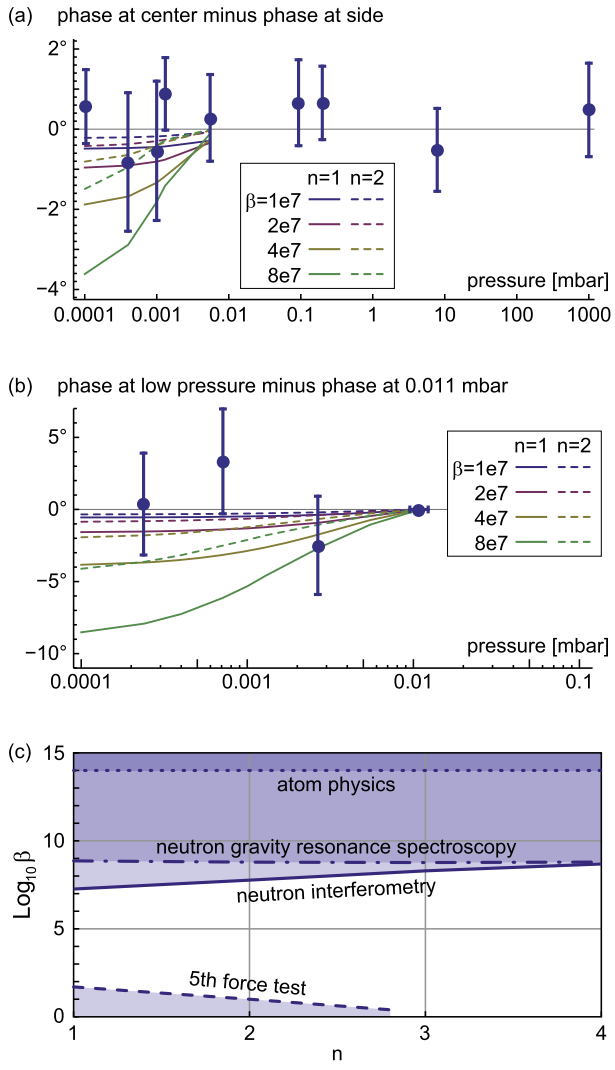


**Fig. 4.** Measured phase shifts in the profile mode (a) and pressure mode (b) compared to calculations for different values of $\beta$ and $n$. (c) Exclusion plot comparing our results with other experiments taken from [16]. The limit for $\beta$ at 95% confidence level is shown for different values of $n$.

(0.011 mbar) as reference and determine the phase shift between this pressure and the other pressure values. The magnitude of the phase shift created by the Helium itself is in the order of $\lesssim 0.001°$ in this pressure range and can be neglected.

## 4. Limit calculation

The solution of the chameleon field in vacuum confined between two walls at $x = \pm d/2$ is given analytically [27] by

$$\varphi_{1D}(x) = \Lambda \left\{ \frac{\Lambda d}{\hbar c} \frac{n+2}{2\sqrt{2}} \left[ 1 - \left( \frac{x}{d} \right)^2 \right] \right\}^{\frac{2}{n+2}}. \tag{3}$$

For higher dimensions and for finite gas pressure the calculation has to be done numerically. The left side of Fig. 1 (c) shows the longitudinal field profile $\varphi_{3D}(x, y = 0, z = 0)$ along the center of the chamber calculated in 3D and for vacuum. It vanishes at the walls and increases towards the middle. Over most of the range it is nearly constant because it is limited by the much narrower transverse confinement. The transverse field distribution $\varphi_{2D}(y, z) \approx \varphi_{3D}(0, y, z)$ is shown on the right side.

Since the full 3D calculation is very time consuming we assume to good approximation that the field depends only on the transverse coordinates. We account for the longitudinal drop close to the walls by calculating an effective chamber length $l_{\text{eff}}$ such that

$$\int_{-l/2}^{l/2} \varphi_{3D}(x, 0, 0)\, dx = \varphi_{3D}(0, 0, 0)\, l_{\text{eff}}. \tag{4}$$

Thus the true length $l = 94$ mm reduces effectively to $l_{\text{eff}} = \{84, 85.6, 86.8, 87.6\}$ mm respectively for $n = \{1, 2, 3, 4\}$. The expected phase shift $\zeta$ given by Eq. (2) simplifies to

$$\zeta = \frac{m}{k\hbar^2}\, \beta\, \frac{m}{M_{\text{Pl}}}\, \varphi_{2D}(y, z)\, l_{\text{eff}} \tag{5}$$

and is plotted in Fig. 4 (a) and (b) assuming various values for $\beta$ and $n$.

We calculate limits for $\beta$ by comparing the calculated phase shifts $\xi$ with the measured phase shifts $\zeta \pm \sigma$. We assume certain values of $\beta$ and calculate the corresponding probability $p$,

$$p(\beta) = \frac{\exp\left[ -\frac{1}{2}\, \chi(\beta)^2 \right]}{\int_0^{\beta_{\max}} \exp\left[ -\frac{1}{2}\, \chi(\beta)^2 \right] d\beta} \tag{6}$$

$$\chi(\beta)^2 = \sum_i \frac{[\xi(\beta)_i - \zeta_i]^2}{\sigma_i^2}. \tag{7}$$

The sum goes over the data points shown in Fig. 4 (a) and (b). We determine the limit $\beta_{\text{lim}}$ with 95% confidence level by numerically solving the equation

$$\int_0^{\beta_{\text{lim}}} p(\beta)\, d\beta = 95\%. \tag{8}$$

The calculation is repeated for different values of $n$ yielding the following results.

$$\beta_{\text{lim}} = \begin{cases} 1.9 \times 10^7\,, & n = 1\,, \\ 5.8 \times 10^7\,, & n = 2\,, \\ 2.0 \times 10^8\,, & n = 3\,, \\ 4.8 \times 10^8\,, & n = 4\,. \end{cases} \tag{9}$$

Both the profile mode and the pressure mode contribute about equally to these limits. For large $n$ the profile mode becomes less sensitive because the bubble shape becomes flatter on the top.

## 5. Conclusion

Our search for chameleons by means of neutron interferometry failed in finding ones but succeeded in deriving new upper bounds for the coupling constant $\beta$, listed in Eq. (9). For $n = 1$ the new limit is a factor of 30 below the previous one which has been obtained by gravity resonance spectroscopy, cf. Fig. 4 (c). There remains a range of five orders of magnitude for $\beta$ where chameleons have not been excluded yet.

## Acknowledgements

We thank Helmut Rauch and Martin Suda for useful discussions and Manfried Faber for theoretical support. We thank Thilo Pirling and Sergio Martinez from the ILL for the thickness mapping.

We gratefully acknowledge support from the Austrian Science Fonds (FWF) under Contracts Nos. I529-N20, I530-N20, I531-N20, I689-N16, I862-N20, and the Collaboration agreement ILL-1132.

## References


[1] E.J. Copeland, M. Sami, S. Tsujikawa, Dynamics of dark energy, Int. J. Mod. Phys. D 15 (11) (2006) 1753–1935, http://dx.doi.org/10.1142/S021827180600942X.

[2] Timothy Cliftona, Pedro G. Ferreiraa, Antonio Padillab, Constantinos Skordisb, Modified gravity and cosmology, Phys. Rep. 513 (2012) 1–189, http://dx.doi.org/10.1016/j.physrep.2012.01.001.

[3] A. Joyce, B. Jain, J. Khoury, M. Trodden, Beyond the cosmological standard model, arXiv:1407.0059 [astro-ph.CO], 2014.

[4] P. Brax, A.-C. Davis, Casimir, gravitational and neutron tests of dark energy, arXiv:1412.2080 [hep-ph], 2014.

[5] A. Upadhye, Dark energy fifth forces in torsion pendulum experiments, Phys. Rev. D 86 (2012) 102003, http://dx.doi.org/10.1103/PhysRevD.86.102003.

[6] P. Brax, C. van de Bruck, A.C. Davis, D.J. Shaw, D. Iannuzzi, Tuning the mass of chameleon fields in casimir force experiments, Phys. Rev. Lett. 104 (2010) 241101, http://dx.doi.org/10.1103/PhysRevLett.104.241101.

[7] P. Brax, G. Pignol, D. Roulier, Probing strongly coupled chameleons with slow neutrons, Phys. Rev. D 88 (2013) 083004.

[8] P. Brax, C. van de Bruck, A.-C. Davis, Compatibility of the chameleon-field model with fifth-force experiments, cosmology, and pvlas and cast results, Phys. Rev. Lett. 99 (2007) 121103, http://dx.doi.org/10.1103/PhysRevLett.99.121103.

[9] P. Brax, C. van de Bruck, A.-C. Davis, D.F. Mota, D. Shaw, Testing chameleon theories with light propagating through a magnetic field, Phys. Rev. D 76 (2007) 085010, http://dx.doi.org/10.1103/PhysRevD.76.085010.

[10] C. Burrage, Supernova brightening from chameleon–photon mixing, Phys. Rev. D 77 (2008) 043009, http://dx.doi.org/10.1103/PhysRevD.77.043009.

[11] C. Burrage, A.-C. Davis, D.J. Shaw, Detecting chameleons: the astronomical polarization produced by chameleonlike scalar fields, Phys. Rev. D 79 (2009) 044028, http://dx.doi.org/10.1103/PhysRevD.79.044028.

[12] A.-C. Davis, C.A.O. Schelpe, D.J. Shaw, Effect of a chameleon scalar field on the cosmic microwave background, Phys. Rev. D 80 (2009) 064016, http://dx.doi.org/10.1103/PhysRevD.80.064016.

[13] A.S. Chou, W. Wester, A. Baumbaugh, H.R. Gustafson, Y. Irizarry-Valle, P.O. Mazur, J.H. Steffen, R. Tomlin, A. Upadhye, A. Weltman, X. Yang, J. Yoo, Search for chameleon particles using a photon-regeneration technique, Phys. Rev. Lett. 102 (2009) 030402, http://dx.doi.org/10.1103/PhysRevLett.102.030402.

[14] G. Rybka, M. Hotz, L.J. Rosenberg, S.J. Asztalos, G. Carosi, C. Hagmann, D. Kinion, K. van Bibber, J. Hoskins, C. Martin, P. Sikivie, D.B. Tanner, R. Bradley, J. Clarke, Search for chameleon scalar fields with the axion dark matter experiment, Phys. Rev. Lett. 105 (2010) 051801, http://dx.doi.org/10.1103/PhysRevLett.105.051801.

[15] J.H. Steffen, A. Upadhye, A. Baumbaugh, A.S. Chou, P.O. Mazur, R. Tomlin, A. Weltman, W. Wester, Laboratory constraints on chameleon dark energy and power-law fields, Phys. Rev. Lett. 105 (2010) 261803, http://dx.doi.org/10.1103/PhysRevLett.105.261803.

[16] P. Brax, G. Pignol, Strongly coupled chameleons and the neutronic quantum bouncer, Phys. Rev. Lett. 107 (2011) 111301.

[17] Y. Pokotilovski, Strongly coupled chameleon fields: possible test with a neutron Lloyd's mirror interferometer, Phys. Lett. B 719 (2013) 341–345.

[18] T. Jenke, P. Geltenbort, H. Lemmel, H. Abele, Realization of a gravity-resonance-spectroscopy technique, Nat. Phys. 7 (2011) 468–472.

[19] H. Abele, T. Jenke, D. Stadler, P. Geltenbort, QuBounce: the dynamics of ultracold neutrons falling in the gravity potential of the Earth, Nucl. Phys. A 827 (2009) 593–595, http://dx.doi.org/10.1016/j.nuclphysa.2009.05.131.

[20] T. Jenke, D. Stadler, H. Abele, P. Geltenbort, Q-bounce experiments with quantum bouncing ultracold neutrons, Nucl. Instrum. Methods Phys. Res., Sect. A 611 (2009) 318–321.

[21] H. Abele, T. Jenke, H. Leeb, J. Schmiedmayer, Ramsey's method of separated oscillating fields and its application to gravitationally induced quantum phase shifts, Phys. Rev. D 81 (2010) 065019, http://dx.doi.org/10.1103/PhysRevD.81.065019.

[22] T. Jenke, G. Cronenberg, J. Burgdörfer, L.A. Chizhova, P. Geltenbort, A.N. Ivanov, T. Lauer, T. Lins, S. Rotter, H. Saul, U. Schmidt, H. Abele, Gravity resonance spectroscopy constrains dark energy and dark matter scenarios, Phys. Rev. Lett. 112 (2014) 151105.

[23] J. Khoury, A. Weltman, Chameleon fields: awaiting surprises for tests of gravity in space, Phys. Rev. Lett. 93 (2004) 171104.

[24] D.F. Mota, D.J. Shaw, Evading equivalence principle violations, cosmological, and other experimental constraints in scalar field theories with a strong coupling to matter, Phys. Rev. D 75 (2007) 063501, http://dx.doi.org/10.1103/PhysRevD.75.063501.

[25] H. Rauch, S.A. Werner, Neutron Interferometry, Clarendon Press, Oxford, 2000.

[26] M. Zawisky, M. Baron, R. Loidl, H. Rauch, Testing the world's largest monolithic perfect crystal neutron interferometer, Nucl. Instrum. Methods Phys. Res., Sect. A: Accelerators, Spectrometers, Detectors and Associated Equipment 481 (2002) 406–413, http://dx.doi.org/10.1016/S0168-9002(01)01253-0.

[27] A.N. Ivanov, R. Höllwieser, T. Jenke, M. Wellenzohn, H. Abele, Influence of the chameleon field potential on transition frequencies of gravitationally bound quantum states of ultracold neutrons, Phys. Rev. D 87 (2013) 105013.